Three-Dimensional Wave Dynamics on a Falling Film and Associated Mass Transfer

C. D. Park and T. Nosoko
Dept. of Mechanical and Systems Engineering, University of the Ryukyus, Nishihara, Okinawa 903-0213, Japan

The evolution of solitary waves into three-dimensional (3-D) waves was experimentally observed on a vertically falling water film at mainly Re = 10–100. At Re greater than 40, 2-D solitary waves are very unstable in the face of spanwise perturbations of approximately 2-cm wavelengths and disintegrate into isolated horseshoe-shaped solitary waves and clusters of dimples between the horseshoes, whereas wavefront modulations are limited to low levels at Re below 40. Horseshoes of larger velocities have larger curvature heads, and extend longer oblique legs upward. Curving capillary ripples preceding each horseshoe widen their wavelengths with an increase in the wavefront inclination, showing that the ripples possess the characteristics of the shallow-water capillary waves. The horseshoes may hold vortices inside, and they have similarities in shape and size to hairpin vortices observed in laminar–turbulent transition regions of boundary layers on walls. The disintegration of waves into dimples is caused by a capillary instability similar to the one for breakup of a cylindrical soap film. This transition of wave dynamics at Re ≈ 40 is associated with a drastic change in the mass transfer from the surface into the film.

Introduction

Liquid films falling down inclined or vertical walls are frequently encountered in natural and industrial processes. The falling films are unstable and surface waves occur on the films when the Reynolds number *Re* (defined in the subsection on mass-transfer coefficient and dimensionless groups) exceeds a critical value. Instabilities of the film flow are convective (Liu et al., 1993; Joo and Davis, 1992a; Cheng and Chang, 1995), and upstream noise perturbations selectively develop into surface waves as they flow downstream (Chang et al., 1996a,b; 2002).

Typical wave evolution when a uniform film is formed on a vertical wall can be seen in Figure 1. Two-dimensional (2-D) deformations become visible on a smooth film surface at some distances from the film inlet, and then rapidly develop into saturated 2-D waves that travel distances of several wavelengths in a quasi-stationary state. During the quasi-stationary motion, separations between these waves gradually become uneven, associated with increases in transverse deformation of their wavefronts. Then adjacent waves interact with each other and coalesce to distort the wavefronts significantly. The resulting distorted waves with large separations increase their distortions further to split the wavefronts.

Correspondence concerning this article should be addressed to T. Nosoko.

Except for the periods of inception and interactions, these 2-D and 3-D waves have surface structures consisting of a single large *teardrop hump* and several small *capillary ripples*, as shown in Figure 2. Each teardrop hump has a steep front to form capillary ripples that exponentially decrease in amplitude with the downstream distance from the front of the hump. Such wave structures are often referred to as "solitary waves" or "solitary humps" (Chang, 1994; Ramaswamy et al., 1996; Liu and Gollub, 1994), because the humps that dominate the dynamics of the wave structures are essentially separated from each other. Whether wavefronts are horizontal, slanting, or curving, the waves retain such teardrop-hump/capillary-ripple structures. Here we mainly review relevant reports on solitary or nearly solitary waves, though close-packed waves also have been extensively studied theoretically and experimentally.

The primary instability causing the inception of 2-D waves on a smooth film surface has been extensively studied through linear analyses of the Navier-Stokes equations by Yih (1963), Benjamin (1957) and other researchers. The instability occurs when the wave number, α, is smaller than a critical value or the cutoff wave number α_c, and with increasing wave number the growth rate of the instability increases to the maximum and then decreases to vanish at α_c. The wave numbers ob-

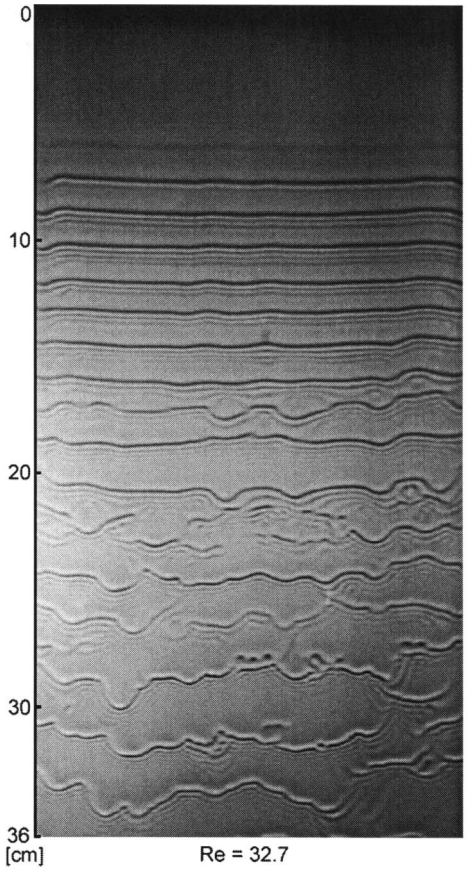

Figure 1. Shadow image of waves naturally occurring on a falling film at $Re = 32.7$ without controlled perturbations imposed on film flow.

Refer to the subsection on surface structures of waves and their shadows, and Figure 2 for the relationship between wave structures and their shadows.

served experimentally at the wave inceptions on smooth surfaces scatter to some extent, and are about or are smaller than the theoretical wave number for the maximum growth rate or the *fastest growing* wave number, α_m (Pierson and Whitaker, 1977).

The steady traveling 2-D waves were constructed at small Re ($Re \approx 15$ or less for vertical water films) and at larger Re through nonlinear long-wave evolution equations reduced from the Navier-Stokes equations by Pumir et al. (1983), Joo et al. (1991), Ooshida (1999), among others, and through the full Navier-Stokes equations or boundary-layer formulas of

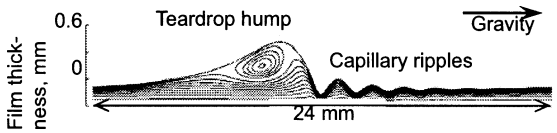

Figure 2. Teardrop-hump/capillary-ripple structure and vortex in the hump constructed by numerical simulation for a vertically falling water film at $Re = 36.6$.

The isoconcentration contours show a vortex in the hump. [A reprint of Figure 5-d by Nagasaki et al. (2002).]

the Navier-Stokes equations by Nagasaki et al. (2002), Nagasaki and Hijikata (1989), Miyara (2000), Ramaswamy et al. (1996), Salamon et al. (1994), Ho and Patera (1990), Tsvelodub and Trifonov (1992), and Chang et al. (1993a,b). Such waves and their dynamics also have been experimentally captured by Kapitza and Kapitza (1965), Alekseenko et al. (1985, 1994), and Nosoko et al. (1996) by imposing pulses at constant frequencies on the inlet film flow. These techniques of controlling temporal upstream perturbations cause 2-D waves to travel in a quasi-stationary state over distances of about ten or more wavelengths. When compared, the results of these theoretical and numerical studies showed good agreement with the experimental observations.

The 3-D secondary instability leading to wavefront deformation has been studied through long-wave evolution equations by Joo and Davis (1992a, b), and through the boundary-layer formulas of the Navier-Stokes equations by Trifonov (1991) and Chang et al. (1994). Their constructions of 3-D waves are limited to small Reynolds numbers ($Re \approx 10$ or less). The 3-D instability has a cutoff transverse wave number, and the instability grows when its wave number is smaller than the cutoff value. The instability grows much more slowly than the primary one, and gradually increases transverse distortions on saturated 2-D waves (Chang et al., 1994). The nearly solitary waves hold surface structures similar to the original 2-D wave structures, even after the transverse distortion has developed (Trifonov, 1991; Chang et al., 1994). Recently Chang and Demekhin (2002) performed a preliminary analysis of 3-D waves at small to large Re through the generalized Kuramoto-Sivashinsky equation, one of the long-wave evolution equations, and showed that the wave structures holding 2-D cross sections with transversely modulated wavefronts are stable at a certain Re range, whereas the wave structures begin to disintegrate into several disconnected 3-D humps at Re beyond that range.

Wave structures analogous to the teardrop-hump/capillary-ripple cross sections, along with their 3-D distributions and time variations, were experimentally observed on films falling down a plane inclined slightly from the horizontal (Liu et al., 1995). It was observed that waves evolve much more slowly on the slightly inclined film than on vertical ones. They showed that when 2-D waves with large constant spacings are excited, transverse modulations of the wavefronts slowly develop and then level off at small transverse amplitudes with about 3-cm transverse wavelengths. When close spaced 2-D waves are excited, the waves coalesce with their neighbors, and eventually teardrop-hump/capillary-ripple structures with rather irregular wavefront modulations become dominant far downstream.

When the waves are restricted to the 2-D, wave coalescence events have been numerically constructed on a long film by Chang et al. (1996a, b; 2002). They showed that solitary humps irreversibly coalesce to form a single large teardrop hump, with associated rapid acceleration and widening of hump separations. The resulting large teardrop humps coalesce several times with front-running smaller teardrop humps in a cascading fashion as they travel downstream.

Mass transfer from the surface into a falling liquid film is strongly dependent on the flow structures in the film, since diffusivities in liquid are very low (Himmelblau, 1964). Sur-

face waves have been found experimentally to cause several-fold increases in the mass-transfer coefficient in falling films (Emmert and Pigford, 1954; Kamei and Oishi, 1956; Seban and Faghri, 1978). The mass-transfer coefficient increases with Re and experimental curves of the coefficient have a break on the log-log scale at $Re = 40-75$ where the slope of the curve sharply decreases (Bakopoulos, 1980; Hikita et al., 1959; Nakoryakov et al., 1983). The break evidently shows that some changes in the dynamics of surface waves occur at the break. Although some have tried to explain such breaks (Nakoryakov et al., 1983; Hikita et al., 1959), the relationship between the mass transfer and the wave dynamics has remained unclear.

Yoshimura et al. (1996) experimentally determined the mass-transfer enhancement caused by 2-D teardrop-hump/capillary-ripple structures on a short vertical water film that was 24 cm high, using the technique of controlling temporal perturbations. With the aid of numerical simulations of 2-D waves by Nagasaki and Hijikata (1989), Yoshimura et al. showed that flow circulation or vortices in the teardrop humps renew the film surface to allow concentration boundary layers to develop along short distances between the teardrop humps, and to be much thinner than the film thickness. The 2-D waves monotonously increase these renewal effects with increasing heights and speeds of the humps. The vortices are so weak that they are visualized with isoconcentration contours in gas-absorbing wave structures, as shown in Figure 2 (Nagasaki et al., 2002) and with streamlines in the coordinates translating with the wave speed (Miyara, 2000). Roberts and Chang (2000) constructed a theoretical model of the mass-transfer enhancement of such vortices in 2-D humps, and explained the experimental observations of a sharp rise in the mass-transfer enhancement with Re increasing from 10 to 40. Recently, Vazquez-Una et al. (2000) found a similar mass-transfer enhancement by surface waves on films flowing on a horizontal plane, and reported that the mass-transfer coefficient monotonously increases with wave amplitude.

Experimental techniques controlling upstream perturbations have often been successfully used in explorations of transitions of boundary-layer flow on walls or in channels, and in the vortex developments in free shear layers (Nishioka et al., 1981; Acardar and Smith, 1987; Lasheras and Choi, 1988). In this work, we employed similar techniques where time-periodic perturbations of constant frequencies and spanwise perturbations of constant intervals were imposed on the inlet film flow on a vertical plane. When such spatiotemporal perturbations of relatively low frequencies are imposed, 2-D waves evolve into 3-D waves with regular behaviors by skipping complicated wave interactions and coalescence. The resulting wavefront patterns were observed by shadowgraphy. Our efforts were mostly confined to observations of such waves at $10 < Re < 100$ to capture the possible changes of the wave dynamics at the break of mass-transfer coefficient curve.

Experimental Methods

Apparatus and procedure

We used two experimental apparatuses to observe surface waves on a film falling down a vertical plane and to determine the mass-transfer coefficient of a film falling inside a vertical tube. For the wave observations, tap water is made to flow through a silicone tube from a head tank into a water-holding compartment at the top of the glass plate where water is horizontally distributed along the plate (Figure 3a). Then water is passed through a uniform-width channel between the glass plate and a stainless steel bar to form a film on the plate. Either a short or a long glass plate is used to form a film on a 20.5-cm-wide and 24.5-cm-long area or on a 20.5-cm × 49-cm area of the plate. Controlled spatiotemporal perturbations can be imposed on the film flow by beating the silicone tube with a speaker-driven thin plate at constant frequencies f, and by putting fine needles in contact with the film along the inlet at constant spanwise intervals, $\lambda_{z,ndl}$. Two types of spatial perturbations are imposed on the film flow by changing the contact angle of the needle surfaces to water. When the contact angle of water on the needle surface is small, the needles pull up the water surface to locally increase the flow rate, which results in *positive* perturbations. Conversely, *negative* perturbations occur when the contact angle is wide, and locally decrease the flow rate. Water temperature and volumetric flow rate are measured at the bottom exit of the apparatus using a T-type thermocouple, a flask, electric balance, and a stopwatch. A flash from a stroboscope passes horizontally through the film and the glass plate, forming shadows of the waves on a screen right behind the plate. A digital camera synchronized with the stroboscope captures the shadows.

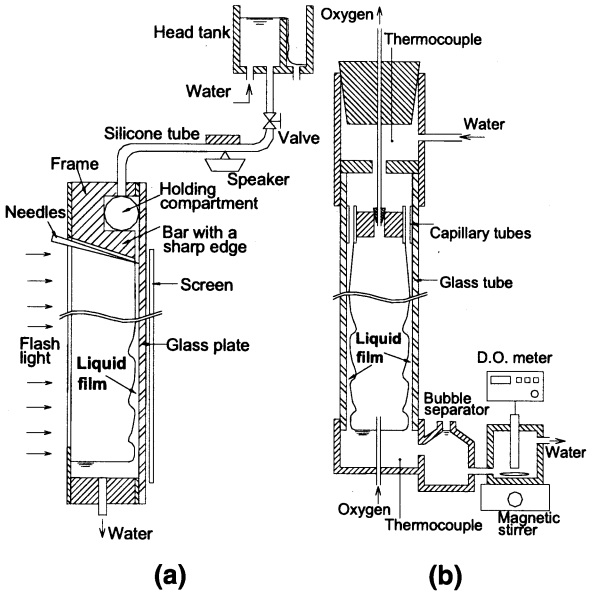

Figure 3. Experimental apparatuses (a) for a film falling down a vertical plane, and (b) for a gas-absorbing film falling inside a vertical tube.

Films falling inside a tube eliminate side-wall effects, which a film on a plane always has. Tap water flows into a two-story compartment, where it is evenly distributed through 17 capillary tubes arranged along the inner wall of the glass tube, which then forms a 95-cm-high film falling inside the glass tube of 9.6-mm inner diameter (Figure 3b). Oxygen gas from a cylinder is fed into the water in a bottle to cause bubbling and then made to flow into the glass tube from its base, leaving the tube from its top. With oxygen gas flowing through

the core space of the glass tube, oxygen rich water and its accompanying oxygen bubbles flow from the bottom of the tube into a bubble-separating bottle, after which bubble-free water flows into the container, where dissolved oxygen concentration C_{out} is measured. Water temperature is measured at the top and the bottom of the tube. The dissolved concentration of oxygen in the water that enters the container directly from the faucet is also measured prior to and immediately after each series of experimental runs. The film temperature, T, and the concentration C_{in} at the film inlet are assumed to be averages of these temperature and concentration measurements, respectively. The experiments of mass transfer were performed at a range of $T = 15$–24°C and $Re = 20$–900.

Mass-transfer coefficient and dimensionless groups

Assuming that the local mass-transfer coefficient is constant along the film, the mean mass-transfer coefficient, k_L, formulated in terms of the logarithmic mean concentration difference, may be given as

$$k_L = \frac{Q}{\pi(d-2\delta)L}\ln\frac{C_s - C_{in}}{C_s - C_{out}}, \tag{1}$$

where Q, d, δ, L, and C_s are the volumetric flow rate in the film, the inner diameter of the glass tube, the mean film thickness, the film height, and the saturated concentration of oxygen, respectively. The increase in surface area due to waves is slight (Fulford, 1964), and therefore the surface area of the film is assumed to be $\pi(d-2\delta)L$ within the acceptable range. The mean film thickness δ for laminar and turbulent flow can be calculated by the correlation for the Nusselt film and by Brauer's (1956) empirical formula, respectively

$$\delta = \left(\frac{3\upsilon^2 Re}{g}\right)^{1/3} \quad \text{for laminar flow} \tag{2}$$

$$\delta = 0.302\left(\frac{3\upsilon^2}{g}\right)^{1/3} Re^{8/15} \quad \text{for turbulent flow} \tag{3}$$

where g and υ are the gravitational acceleration and the kinematic viscosity of liquid, respectively.

The Reynolds number Re, the Sherwood number Sh, and the Schmidt number Sc are defined as $Re = \Gamma/\upsilon$, $Sh = k_L\upsilon/D$, and $Sc = \upsilon/D$, respectively, where Γ and D are volumetric flow rate per unit length of wetted perimeter and mass diffusivity, respectively. The physical properties υ, D, and C_s are functions of the film temperature T. Values for υ are available from the Data Book (JSME, 1986), and values for D and C_s were derived from the Stokes-Einstein equation (referred to in Bird et al., 1960), with $D = 2.341\times10^{-9}$ m^2/s at $T =$ 25°C (Himmelblau, 1964), and from the correlation by Truesdale et al. (1955), respectively. The saturated vapor pressure of water reduces the partial pressure of oxygen at the film surface and C_s, and this reduction is calculated from Henry's law to determine the C_s.

Surface structures of waves and their shadows

When light rays pass through wave valleys and ridges, the rays diverge and converge onto the screen behind the film, respectively. Hence, a teardrop-hump/capillary-ripple structure forms a set of dark and bright strips on the screen, as shown in all snapshots in this article. The valleys have larger curvatures on bottoms than those on the neighboring ridges (see Figure 2), and therefore darker strips are more noticeable than the bright ones. While the deepest valley in front of the teardrop hump distinctly forms the darkest strip among the set of strips, the valleys of capillary ripples farther from the teardrop hump form less dark strips with decreasing amplitudes. Likewise, higher peak teardrop humps form deeper valleys in front of them, resulting in darker strips on the screen. These distinctive dark strips of the deepest valleys may represent the wavefronts of teardrop humps. As a result, the shadows of waves may show transverse variations of wavefronts; separations between teardrop humps, λ_{hmp}; the number of capillary ripples preceding each teardrop hump; the wavelengths of the capillary ripples; qualitatively the peak heights of the teardrop humps and the amplitudes of the capillary ripples.

Results and Discussion

Mass-transfer enhancement by surface waves

A measured variation of the Sherwood number Sh with the Reynolds number Re is compared in Figure 4 with the empirical correlations by Bakopoulos (1980) and with a solution to the equation of diffusion into a smooth surface film of a semiparabolic velocity profile by Tamir and Taitel (1971). Bakopoulos constructed the correlations to fit the data measured with vertical long water films (mostly film heights of 1 m or higher) by Emmert and Pigford (1954), Kamei and Oishi (1956), Hikita et al. (1959), and Lamourelle and Sandall (1972). Tamir and Taitel's solution changes the relationship between Sh and Sc with the ratio of film height to film thickness, and here an average value of the present measurements, $Sc = 479$, was employed to draw the curve of the solution in Figure 4 for comparison.

The experimental data show that the increase in Sh is rapid in $Re < 40$, gentle in $40 < Re < 400$, and then rapid in $Re >$

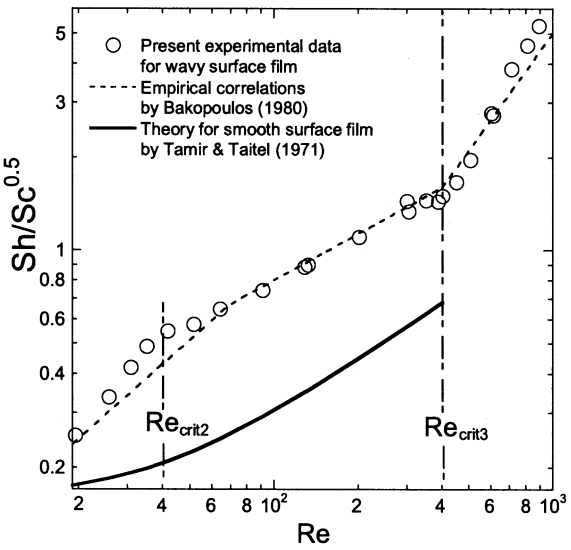

Figure 4. Mass-transfer enhancement by surface waves and two breaks of mass-transfer curve.

400, showing two breaks at $Re \approx 40$ and 400. The slopes of the data are approximately 1.0, 0.5, and 1.4 in $Re < 40$, $40 < Re < 400$ and $Re > 400$, respectively. Since the mean film thickness δ increases with Re, as described by Eqs. 2 and 3, the mass-transfer coefficient k_L is in proportion to $Re^{2/3}$, $Re^{1/6}$, and $Re^{4/5}$ in $Re < 40$, $40 < Re < 400$, and $Re > 400$, respectively, showing very weak dependence of k_L on Re in $40 < Re < 400$. The present data are in good agreement with the correlations by Bakopoulos in $Re > 75$, but are a little larger in $Re < 75$. The experimental data, which he collected for the correlations, scatter to some extent, and the present measurements fall within the scattering.

A break occurs at $Re \approx 400$ on both the present data and the correlations by Bakopoulos, and it may represent a transition from wavy laminar flow to turbulent flow. Brauer (1956), Feind (1960), and Emmert and Pigford (1954) determined that the transition occurs at $Re \approx 400$, based on their measurements of variations of film thickness, wall shear stress, and mass-transfer coefficient with Re, respectively. The present measurements are in good agreement with their findings.

Another break occurs at $Re \approx 40$ and 75 on the present data and on the correlations by Bakopoulos, respectively. Likewise, Emmert and Pigford (1954), Hikita et al. (1959), and Nakoryakov et al. (1983) reported such breaks in $40 < Re < 75$. Jackson (1955) proposed the "turbulent wave" concept, where turbulence is localized within peak regions of solitary waves, which travel downstream on a laminar substrate film. Hikita et al. tried to explain the break of the mass-transfer curve with the aid of the turbulent-wave concept. Recent numerical simulations have denied such localized turbulence at low Re (Nagasaki et al., 2002; Miyara, 2000).

Comparison of the present Sh data with the solution by Tamir and Taitel (1971) shows that surface waves rapidly increase the mass-transfer coefficient, k_L, with Re up to 2.6 times the solution at $Re = 40$, associated with large differences in the slope, and then gently increase k_L with a small slope to 2.2 times the solution at $Re = 400$. Emmert and Pigford (1954), Kamei and Oishi (1956), Hikita et al. (1959), Seban and Faghri (1978), and Nakoryakov et al. (1983) also reported similar increases in mass-transfer coefficients caused by surface waves.

Figure 5 shows the shadows of the waves on a water film falling inside the vertical tube. As flashlight rays pass horizontally through the vertical circular tube, the shadows of waves on two narrow areas of the film are enlarged due to the curvature of the tube wall and projected together on the screen. Because these shadows cause some difficulties in observing the wave dynamics, we provide a brief overview of the wave dynamics in this section.

2-D waves appear on a smooth surface at distance $x \approx 6$ cm at $Re = 20.4$ from the film inlet (Figure 5). These waves then demonstrate increasing distortions of their wavefronts, associated with wave interactions and coalescence, which cause drastically increasing wave separations and much more wavefront distortion (an increase in wave separation due to such coalescence and adjacent waves in interaction are observed at $x \approx 19$ cm and 30 cm at $Re = 20.4$ in Figure 5). At larger Re, wave inception occurs further downstream, and the first wave interaction event occurs at a shorter distance from the inception (at $Re = 40.2$, 64.2, and 200 in Figure 5). The wave interactions appear to become more complex with increasing Re, and highly 3-D waves holding continuous wavefronts become dominant downstream after the wave interactions at $Re < 200$. At $200 < Re < 400$, nearly isolated *depressions* appear on the smooth surface (Figure 5), and 3-D waves with distorted wavefronts seem to eventually become dominant far downstream. Waves never appear at Re above 400, but isolated depressions are dominant throughout the film surface downstream from their inception. With increasing Re, from 400 to 700 depressions appear more upstream on the smooth surface, and the smooth surface becomes rougher. The smooth surface area disappears and the whole film surface is covered with depressions at Re above 700. This rapid upstream shift of the depression inception and the dominant depressions on the downstream surfaces seem to be caused by the transition to turbulent flow in the film, along with the break of the mass-transfer curve at $Re \approx 400$ (Figure 4).

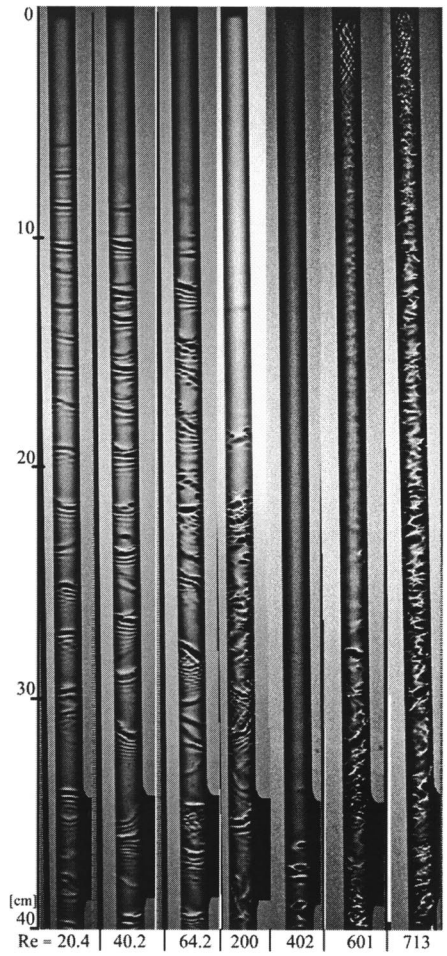

Figure 5. Shadow images of waves on films falling inside a glass tube.

The images capture the films at $x = 0$–40 cm.

Evolution of waves into 3-D waves

The dynamics of waves can be observed in detail from shadows of films falling down a vertical plane. Shadows of surface waves on a downstream region after their inception are shown in Figure 6, where wavefront patterns at Re below

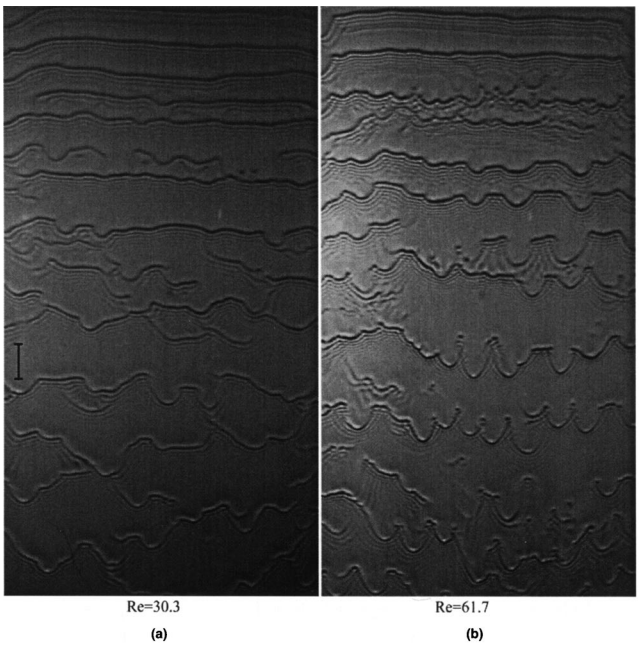

Figure 6. Shadow images of waves without controlled perturbations imposed on film flow.

The images capture the films at $x = 14-48$ cm, and the bar is 2 cm long.

40 are compared with those at *Re* above 40. Since 2-D solitary waves occur with random wave numbers and random velocities around the fastest growing wave number, α_m, and velocity, respectively, they gradually change separations between them, growing transverse modulations of their wavefronts, after which interactions of adjacent waves occur at some distance from their inception (a typical wave interaction is seen between the third and the fourth waves from the top in Figure 6b). When two solitary waves come close, they either almost merge along their wavefronts, or they rapidly increase the transverse modulations of their wavefronts and partially merge at several points. In the latter case, the upper wave weakens and decelerates to detach its wavefront from the merging parts and to leave its partner (see the sixth wave from the top in Figure 6a). The next upstream wave catches up to absorb these disconnected waves, which greatly distorts its wavefront. After such wave interactions, including wave coalescence, 3-D wavefront patterns with large wave separations appear downstream.

The 3-D wavefront patterns are different between *Re* below 40 and *Re* above 40, that is, the wavefront patterns at *Re* above 40 are distinct from those at *Re* below 40 by a large number of horseshoe-shapes, each consisting of a large curvature head and two oblique legs extending upward from the head and by dimples at the ends of the legs. Several shapes similar to those horseshoes appear on the wavefronts at *Re* below 40, but they do not develop into fully developed horseshoes nor accompanying dimples.

Although at *Re* under 40 isolated single depressions similar to the dimples appear in the course of the wave interactions, they may have development scenarios different from those of the dimples at the ends of the horseshoe legs. Partial coalescence of adjacent humps causes sharp bends in the wavefronts, and the deep valleys in front of the humps deepen at the ends of the sharp bends and disintegrate into isolated depressions. Liu et al. (1995) observed similar birth scenarios of such depressions on films falling down a plane inclined slightly from the horizontal. The birth scenarios of the dimples at the ends of horseshoe legs will be described in the subsection on the structure of the horseshoe and partial wave disintegration.

When the controlled spatiotemporal perturbations are imposed on the inlet film flow at constant low frequencies and at constant spanwise intervals, solitary 2-D waves develop into 3-D waves with regular behaviors (Figure 7), skipping the complex interactions of waves. These waves may demonstrate the differences of the wave dynamics between *Re* below 40 and above 40. At $Re \approx 20$, solitary waves are unstable to 3-D perturbations of spanwise intervals of $\lambda_{z,ndl} \approx 3$ cm or larger. Wavefronts gradually increase their modulation amplitudes of transverse wavelengths $\lambda_z \approx 3$ cm or larger, and then saturate the modulations to have nearly sinusoidal shapes, that is, the shapes of the wavefronts are asymmetrical with upward curvatures smaller than downward curvatures (Figure 7b). The waves are not unstable to the perturbations of $\lambda_{z,ndl} \approx 1$ cm or smaller. When transverse perturbations of $\lambda_{z,ndl} \approx 1$ cm or smaller are imposed, the waves decrease the perturbations but gradually increase the amplitudes of transverse modulations of $\lambda_z \approx 3$ cm and larger wavelengths (Figure 7a). The cutoff transverse wavelength seems to decrease with increasing *Re*.

At *Re* above 40, waves are highly unstable in the face of 3-D perturbations of smaller spanwise intervals of $\lambda_{z,ndl} \approx 2$ cm, and continuously evolve transverse wavefront modulations. The wavefront show sinusoidal shapes with small amplitudes at the first stage. Curves bulging downward on the sinusoids then continuously expand into horseshoe-shapes, while those bulging upward flatten out and then reduce the widths of the flat parts (Figure 7d). Finally, the horseshoes extend their legs and split the legs off the flat parts, which disintegrate into clusters of dimples. The horseshoes keep holding the teardrop-hump/capillary-ripple structures (Figures 7d, 7e and 9). When spanwise perturbations of $\lambda_{z,ndl} = 1$ cm are imposed on the film flow at $Re \approx 90$, the downward curves at 2-cm intervals on the wavefronts grow more rapidly, developing into horseshoes at 2-cm intervals associated with the disintegration of slowly growing curves between the horseshoes into the dimples (Figure 7e). At larger *Re*, the downward curves at 1-cm intervals grow so rapidly that horseshoes occur at random intervals of 1 cm, 2 cm, or values in between. These observations show that the fastest growing transverse wavelength is somewhere near 2 cm at *Re* above 40, and it slightly decreases with increasing *Re*.

At *Re* near and below 40, the sinusoidal wavefront modulations are followed by the evolution of curves bulging downward, with upward curves flattening out between the downward curves (Figure 7c). The evolution of the downward curves then becomes saturated and the waves travel downstream in a quasi-stationary state, showing that deformations of the wavefronts are limited to low levels.

This surface wave behavior changes with the frequency of the imposed perturbations. High-frequency perturbations excite closely packed waves and cause them to transform into

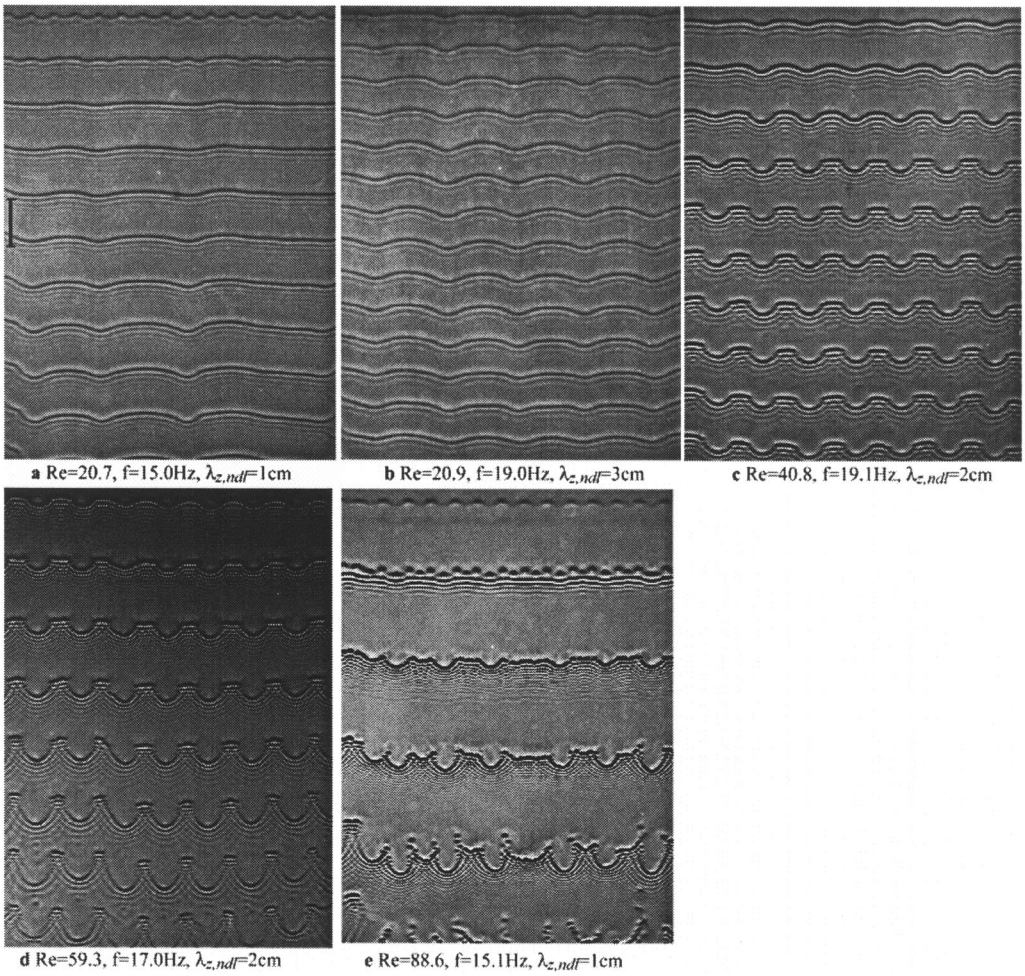

Figure 7. Shadow images of waves excited with controlled spatiotemporal perturbations of constant frequencies *f* and constant spanwise intervals $\lambda_{z,ndf}$.

highly 3-D solitary waves with large separations after complex interactions and coalescence. At very low frequencies, the waves are excited by large separations, and a new wave rapidly develops between the former waves. Then complex interactions and coalescence occur between the former and the latter, causing highly 3-D wavefront patterns. The wave behaviors described in this article are observed at the frequencies where waves are excited to have mostly separations of $\lambda_{hmp} = 2-5$ cm. Naturally occurring 3-D waves seem to have comparable wavelengths after wave coalescence events (Figure 6).

Chang and Demekhin (2002) carried out a preliminary stability analysis and numerical experiments in a wide range of *Re* by solving the 3-D generalized Kuramoto-Sivashinsky equation, and presented four wave-dynamics regimes. The second and third wave regimes seem to predict the previously mentioned experimental observations of 3-D wave behaviors. At the *Re* range of the second regime, 2-D humps develop transverse modulations to some limiting levels without disintegration, whereas the disintegrations of humps into disconnected 3-D humps, or *scallop waves*, occur at larger *Re* in the third regime.

Transverse propagation of wavefront modulation

A single positive perturbation causes a single curve to bulge downward on every 2-D wavefront. This curve then increases in its spanwise width, but not in its height, to induce a gentle modulation with large transverse wavelengths of $\lambda_z \approx 4$ cm at *Re* near 20 or smaller (Figure 8a). The modulations propagate transversely on wavefronts in different behaviors at *Re* above 20 (Figure 8b). Two curves appear on the both sides of the first one excited by the perturbation, and then two more appear on the sides of the second ones. All curves eventually evolve into horseshoes at intervals of about 1.5−2.0 cm at *Re* above 40, but the evolution of the curves saturates at *Re* near 40 or smaller.

A single negative perturbation excites a single bend of the wavefront, followed by the flat top of the bend expanding horizontally at *Re* near 20 or smaller (Figure 8c). The expan-

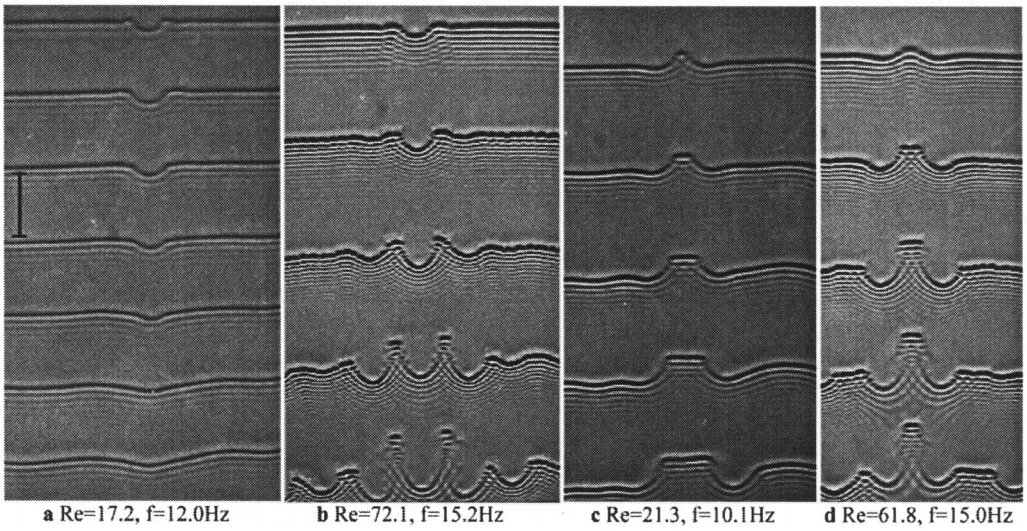

Figure 8. Shadow images of waves excited with single positive (a, b) or negative (c, d) spatial perturbations and time-periodic perturbations.

sion of the flat top is soon saturated at *Re* near 40. At *Re* above 40, the bend with the short flat top accompanies the growth of the downward curves on both sides, coupled with the eventual splitting of the flat top off the two curves. This expansion of the flat part indicates that the waves are not unstable in the face of this single-point perturbation at *Re* near 20 or smaller.

Structure of horseshoe and partial wave disintegration

Horseshoes have gently curving heads that extend oblique legs to short distances upward at *Re* near 40. However, they demonstrate an increase in the head curvatures and elongation of the oblique legs to greater distances at a larger *Re*, as shown in Figure 9. The horseshoes have teardrop-hump/capillary-ripple structures throughout their wavefronts even after they increase the curvatures of the heads and extend the long oblique legs. The horseshoe speed, c, is calculated to be a multiple of the constant frequency, f, and the separation λ_{hmp} between the humps, and variations of the separation λ_{hmp}, which represent variations of the speed c, are shown in Figure 10. The horseshoe heads and the flat parts between them first accelerate to the maxima as the horseshoes are growing, and then gradually decelerate as the horseshoes split off the flat parts that disintegrate into dimples. The heads accelerate faster than the flat parts, which increases the difference in speed between the heads and the flat parts, and the maximum speeds of the heads are slightly higher than those of the fully developed 2-D humps, whereas the flat parts have slightly lower speeds. The heads decelerate to speeds that are slightly lower than those of the 2-D

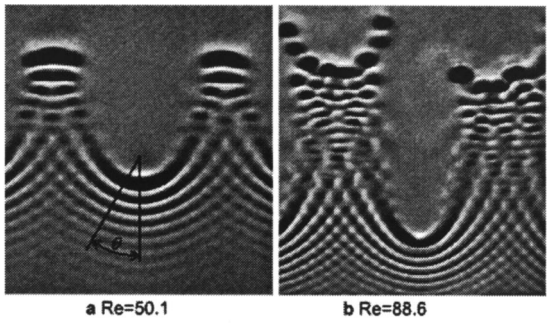

Figure 9. Enlarged images of horseshoe-shaped waves and wave disintegrations into dimples between the horseshoes at $\lambda_{z,ndl} = 2$ cm.

Dark horseshoe-shaped strips represent valleys of capillary ripples, and clusters of dark spots represent the dimples.

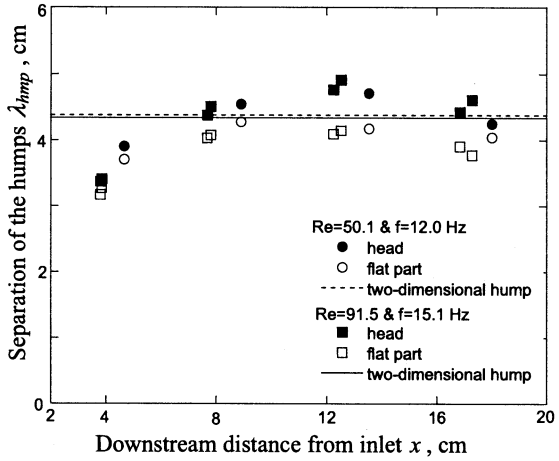

Figure 10. Downstream distance and variations of separation λ_{hmp} of horseshoe heads and of flat parts between the horseshoes at constant frequencies.

The separations between fully developed 2-D waves are calculated at the corresponding values of *Re* and f from the empirical correlation by Nosoko et al. (1996).

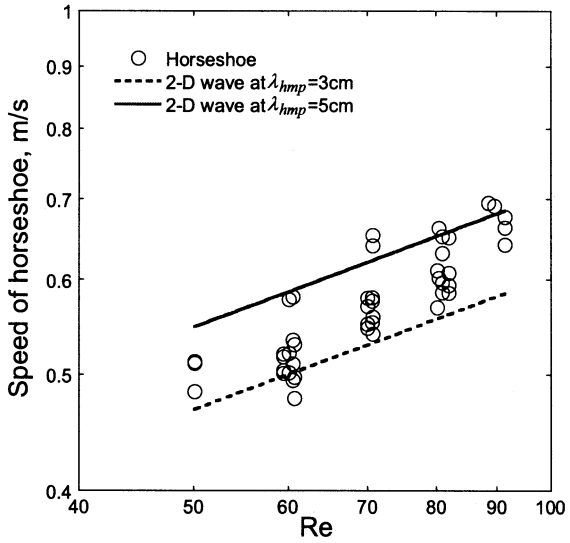

Figure 11. Variation of horseshoe-shaped wave speed with *Re*.

humps. The speeds of the horseshoes increase with *Re* for the constant separations, and they mostly fall between the speeds of the 2-D humps at $\lambda_{hmp} = 3$ cm and 5 cm (Figure 11). The head curvature of the horseshoe also increases with *Re*, and therefore the radius of the head decreases with the speed (Figure 12). Thus, the horseshoes with higher speeds have a greater number of preceding capillary ripples of the smaller wavelengths and larger curvature heads.

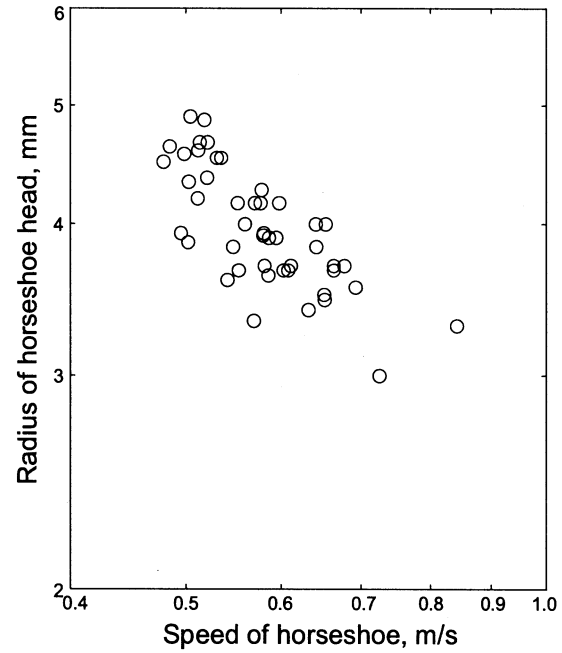

Figure 12. Variation of radius of horseshoe-head wavefront with its speed.

The radii are measured on the darkest strips of shadows, which represent the deepest front valleys and wavefronts of horseshoes.

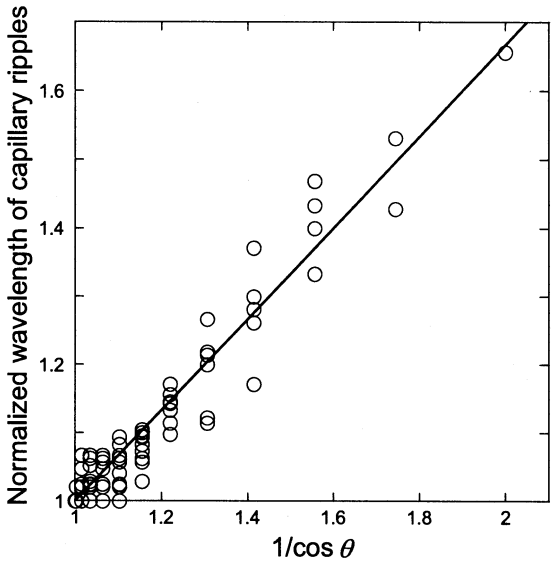

Figure 13. Linear relationship between wavelength λ_{rpl} of capillary ripples and 1/cos θ.

The wavelengths are normalized with respect to wavelengths at $\theta = 0$. The data are presented for $Re = 50$–89 at $f = 12$–15 Hz. The line is drawn to fit the data, passing through (1,1).

Each horseshoe-shaped teardrop hump forms leading capillary ripples that curve along the hump (Figure 9). The capillary ripples are the most closely packed in front of the head of the teardrop hump, and the wavelengths of the ripples increase as the wavefront inclination, θ, increases with distances along the hump from the center of the head toward the ends of the legs. The wavelength of capillary ripples is inversely proportional to cos θ, as shown in Figure 13, where θ is the angle between the normal to the curving wavefront and the vertical (see Figure 9). The linear increase in the capillary ripple's wavelength with 1/cos θ is explained as the following by invoking the theoretical correlation of capillary waves on shallow water (Dias and Kharif, 1999), which shows that the wavelength is inversely proportional to the propagation velocity when the water depth is smaller than the wavelength. A horseshoe-shaped hump travels in the vertical direction at a speed c, and its steep front is sufficiently large to form capillary ripples on the thin residual film behind the leading hump. The hump looks as if it *pushes* the ripples (Brauer, 1956). Unlike the hump, the capillary ripples are *wave* and are not mass-carrying, and therefore two oblique ripples cause *interference* that produces checkerboard patterns on the substrate films between the neighboring horseshoes (Figure 9), where the valleys and crests of the ripples are, respectively, deepened and raised at their intersections. The capillary ripples *propagate* in a direction that is perpendicular to their wavefronts, that is, the directions of angles, θ, with the vertical, though they are *pushed* in the vertical direction at the speed, c, of the horseshoe. As a result, the propagation velocity of the capillary ripples is calculated to be a multiple of c and cos θ. The depth of the substrate film is smaller than the wavelength of the ripples, as shown in Figure 2, and finally the theoretical correlation (Dias and Kharif, 1999) can be applied to the capillary ripples of the

horseshoe to derive the linear increase in the ripple's wavelength with $1/\cos\theta$.

Interference also occurs between the flat capillary ripple and the two oblique capillary ripples, respectively, that precede the flat part and the horseshoe legs (Figure 9). When the flat parts are not too short, dimples appear on the deepest valleys of the flat parts due to *capillary instability* (described in the next subsection), which is associated with the wave interference (Figure 9b). The resulting clusters of dimples decelerate and split off the horseshoe legs (Figure 8d). Then the teardrop hump of the short flat wavefront and the preceding dimples gradually diminish, some of them fading away before the upstream hump catches up with them. At *Re* near 70 or larger, the capillary instability is so intense that the flat deepest valleys disintegrate into rows of dimples, releasing a few dimples from both ends of each row (Figure 9b). When the flat parts are short, such dimples do not appear on the deepest flat valleys (Figure 9a). Instead, the widths of the flat parts decrease.

The horseshoe shadows show that sharply slanting legs still hold teardrop-hump/capillary-ripple structures, but the legs form lighter strips on the screen, since the amplitudes of the capillary ripples and the heights of the hump peaks are much smaller than those of their head parts. The peak height of a teardrop hump monotonously decreases with the distance along its wavefront from the center of the head to the ends of the two legs. Teardrop humps of larger peaks form deeper valleys in front of the peaks as well as larger numbers of leading capillary ripples (Figure 9).

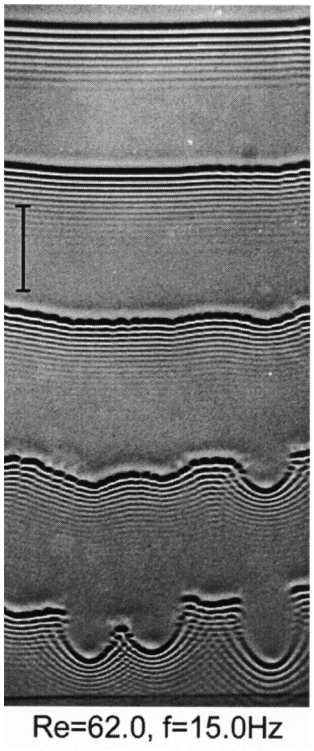

Figure 14. Shadow images of waves excited with time-periodic perturbations and of dimples appearing on 2-D deep valleys.

The snapshot captures the films at $x = 4.6$–21.1 cm, and the bar is 2 cm long.

Capillary instability on deep valley

Dimples also appear on the deepest horizontal valleys in front of the teardrop humps at *Re* above 50, as shown in Figure 14. When only the temporal perturbations are imposed but the spanwise perturbations are not, transverse wavefront modulations start to grow later. At the final stage of 2-D wave development, dimples appear at nearly constant intervals on the deepest valleys, and then quickly spread throughout the valleys before transverse wavefront modulations become significant. Afterwards, the wavefronts increase the transverse modulation that develops into horseshoes at irregular transverse intervals and irregular growth rates, since spatial perturbations can originate from minute defects in the channel discharging the film and trigger the horseshoes. The dimples disappear on the curving heads of horseshoes, whereas they survive or are intensified on the horseshoe legs and on the flat parts between the horseshoes. The flat parts eventually split off from the horseshoes and disintegrate into dimples.

The valleys in front of teardrop humps deepen to form large surface curvatures at their bottoms, which causes liquid-side negative pressure to build up due to capillary force, resulting in the occurrence of a new instability. This instability is basically the same as the capillary instability observed with cylindrical soap films and cylindrical liquid streams that demonstrate necking at constant wavelengths and eventual breakup into bubbles and droplets, respectively (Carroll and Lucassen, 1974). The transverse wavelength, $\lambda_{z,dmp}$, of this instability, that is, the intervals between the dimples, is comparable to and in proportion to the streamwise wavelength, λ_{rpl}, of the capillary ripples, as $\lambda_{z,dmp} = 1.15\ \lambda_{rpl}$ (Figure 15). The fastest growing wavelength of a cylindrical soap film or a liquid stream is proportional to the radius of the cylinder (Boys, 1959; Rumscheidt and Mason, 1962; Carroll and Lucassen,

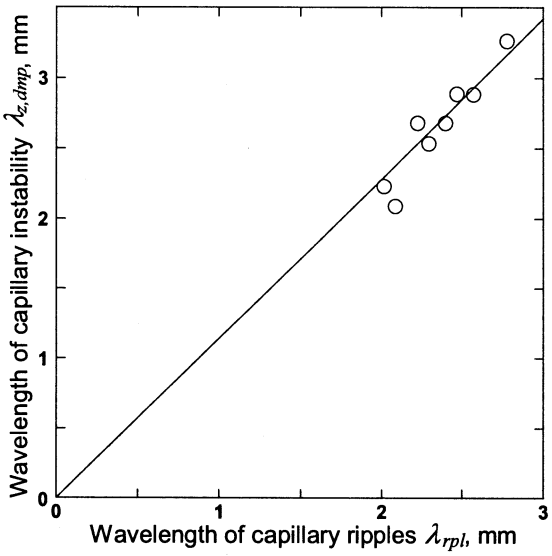

Figure 15. Linear relationship between wavelength of capillary instability $\lambda_{z,dmp}$ and wavelength of capillary ripples λ_{rpl}.

The λ_{rpl} is determined by measuring the streamwise distances between the deepest valley and the next one. The correlation $\lambda_{z,dmp} = 1.15\lambda_{rpl}$ fits the experimental data.

1974). The linear relationship between $\lambda_{z,dmp}$ and λ_{rpl} shows that the deepest valleys have radii on their bottoms that are in proportion to λ_{rpl}.

As mentioned earlier, the dimples disappear on the curving horseshoe heads (Figure 14), and the radii of the horseshoe heads are comparable to the capillary constant of water ($= 3.8$ mm) (see Figure 12), implying that the curvatures of the heads cause additional capillary pressure around the deepest valleys in front, which suppresses the capillary instabilities.

Similarities to hairpin vortices

The horseshoe-shaped humps have some similarities to the hairpin vortices developed in the laminar–turbulent transition regions of the boundary layers on walls. First, the horseshoes are similar in shape to the hairpin vortices during the early stages of development. Second, the distance between the two legs of each horseshoe is comparable to the distance between the two legs of each hairpin vortex. Krist and Zang (1987) constructed the birth of hairpin vortices in plane Poiseuille flow by analyzing computer simulation data. The top views of their hairpin vortices are similar in shape to those of the horseshoe-shaped humps presented here, though the hairpin vortices lift their head up off the wall so their legs make an angle with the wall. A few reports are available on experimental observations of the distance between the two legs of a hairpin vortex. Acarlar and Smith (1987) presented visualizations of counterrotating legs of hairpin vortices in a boundary layer on the wall at a momentum thickness Reynolds number of $Re_\theta = 135$, and Nishioka et al. (1981) reported measurements of velocity fluctuations caused by hairpin vortices in plane Poiseuille flow at $Re_\theta = 667$. Their visualizations and measurements show that the distances between the legs are approximately 1 cm. We measured spanwise distances between horseshoe legs at their ends and found that the distances are in the 0.9–1.6-cm range. These similarities may just be common characteristics of vortices subjected to near-wall shear flow, though such similarities disappear during the later stages when the hairpin vortices continue to grow, extending long streamwise legs, whereas the development of the horseshoe-shaped humps is limited to much smaller levels due to capillary force. The $Re = 40$, equal to $Re_\theta = 8$, for the horseshoe humps is much smaller than the Re_θ for the hairpin vortices, suggesting that the effects of gravity that destabilize the 2-D humps are significant.

Wave dynamics and the associated mass transfer

It is interesting to note that there are large differences in the dynamics of surface waves between Re below 40 and above 40, and at the critical value of $Re \approx 40$, the slope of the $Sh - Re$ curve sharply changes. The waves at Re above 40 are distinguished from the waves at Re below 40 by the development of horseshoe waves and by wave disintegrations between the horseshoes into dimples. The horseshoes have the teardrop-hump/capillary-ripple structure (Figure 2), though the peaks of teardrop humps become smaller on the oblique legs of the horseshoes. Nagasaki et al. (2002) and Miyara (2000) demonstrated that weak vortices occur in teardrop humps. Yoshimura et al. (1996) showed that the vortices renew the film surface to greatly increase the mass transfer from the surface into the film, and these renewal effects monotonously increase with increasing height of the teardrop hump peak. Their findings may not be limited to 2-D waves as long as surface waves hold teardrop-hump/capillary-ripple structures. The wave disintegrations between horseshoes destroy the teardrop-hump/capillary-ripple structures, as well as the vortices inside the teardrop humps. At larger Re, the horseshoes have more sharply curved heads and longer oblique legs where the heights of the teardrop hump peaks are smaller than those of the heads, indicating that these low-peak teardrop humps hold vortices of low intensities. The partial destruction of the vortices and the diminishing vortices along the oblique wavefronts seem to be the main reasons why the slope of $Sh - Re$ curve is much smaller at $40 < Re < 400$ than at $Re < 40$.

Summary and Concluding Remarks

Although it is known that surface waves on falling films eventually become 3-D solitary waves downstream, their behaviors have not been fully understood. This article attempts to describe some features of the surface-wave dynamics on liquid films falling down a vertical plane. The experimental technique of controlling spatiotemporal perturbations allowed surface waves to develop into 3-D waves at regular behaviors (Figure 7). A transition of the wave dynamics occurs at $Re \approx 40$. At Re below 40, 2-D waves are stable in the face of transverse perturbations of short wavelengths, but are unstable to long spanwise perturbations of about 2 cm or larger wavelengths, and develop transverse modulations of their wavefronts up to low levels (Figures 7a to 7c). At Re above 40, 2-D waves convert their wavefront modulations into a number of horseshoe-shapes, which afterward cause the waves between the horseshoes to disintegrate into clusters of dimples (Figures 7d and 7e). The horseshoes continue to hold the teardrop-hump/capillary-ripple structures, with teardrop hump peaks decreasing along the oblique horseshoe legs (Figure 9). The horseshoe-shaped teardrop humps have larger curvature heads (Figure 12) and longer oblique legs at larger Re. The leading capillary ripples curving along a horseshoe increase their wavelengths with an increase in the ripple's wavefront inclination (Figure 13) as predicted by the linear theory of capillary waves on shallow water. Interference between a flat capillary ripple and two oblique capillary ripples occurs on substrate films between horseshoes, and capillary instabilities cause dimples on horizontal deep valleys in front of teardrop humps in the same way that a cylindrical soap film breaks up into a row of bubbles (Figures 14 and 15). The wave interferences and capillary instabilities cause clusters of dimples between the horseshoes, which eventually disintegrate and fade away. The horseshoe-shaped waves are similar in shape and size to hairpin vortices at their birth observed in the laminar–turbulent transition regions of boundary layers and of Poiseuille flow.

In the absence of controlled perturbations, waves appear on a smooth surface, soon causing complex interactions and coalescence between adjacent waves that develop into highly 3-D waves downstream (Figures 1 and 6). The 3-D waves at Re above 40 are distinguished from the waves at Re below 40 by a large number of horseshoes and dimples, suggesting that

the features of the dynamics are basically the same as those of 3-D waves excited by the controlled perturbations.

Measurements of gas absorption into a falling film show that surface waves greatly enhance mass transfer, and that *Sh* increases with *Re* with a slope of 1.0 on a log-log scale at *Re* below 40, whereas the slope sharply decreases at $Re \approx 40$ to be 0.5 in $40 < Re < 400$ (Figure 4). Numerical simulations of film flow by Nagasaki et al. (2002) and Miyara (2000), and the experimental observations of the wave dynamics and the mass transfer by Nosoko et al. (1996) and Yoshimura et al. (1996) suggest that teardrop humps contain swirls or weak vortices inside (Figure 2) that greatly enhance the mass transfer from the surfaces into the films. The wave dynamics mentioned earlier suggest that the initial rapid increase in *Sh* is spoiled at *Re* above 40 by the destruction of the vortices between horseshoes and the diminishing vortices in the oblique horseshoe legs.

Further investigations are required to fully understand the 3-D flow structures in the horseshoes, including the vortices. Numerical simulation techniques (Nagasaki et al., 2002) and velocity profile measurement methods (Karimi and Kawaji, 1998) developed recently seem to be useful in aiding such an understanding of flow structures.

Acknowledgment

This work was supported by The Ministry of Education, Culture, Sports, Science and Technology. We thank S. T. Ro, T. Nagata, K. Oyakawa, Y. H. Mori, and T. Nagasaki for suggestions.

Literature Cited

Acardar, M. S., and C. R. Smith, "A Study of Hairpin Vortices in a Laminar Boundary Layer. Part 2. Hairpin Vortices Generated by Fluid Injection," *J. Fluid Mech.*, **175**, 43 (1987).

Alekseenko, S. V., V. E. Nakoryakov, and B. G. Pokusaev, *Wave Flow of Liquid Films*, Begell House, New York (1994).

Alekseenko, S. V., V. E. Nakoryakov, and B. G. Pokusaev, "Wave Formation on a Vertical Falling Liquid Film," *AIChE J.*, **31**, 1446 (1985).

Bakopoulos, A., "Liquid-Side Controlled Mass Transfer in Wetted-Wall Tubes," *Ger. Chem. Eng.*, **3**, 241 (1980).

Benjamin, T. B., "Wave Formation in Laminar Flow Down an Inclined Plane," *J. Fluid Mech.*, **2**, 554 (1957).

Bird, R. B., W. E. Stewart, and E. N. Lightfoot, *Transport Phenomena*, Wiley, New York (1960).

Boys, C. V., *Soap Bubbles and the Forces which Mould Them*, Doubleday Anchor Books, New York (1959).

Brauer, H., "Stromung und Warmeubergang bei Rieselfilmen," VDI, Forschungshelt, Vol. 457 (1956).

Carroll, B. J., and J. Lucassen, "Effect of Surface Dynamics on the Process of Droplet Formation from Supported and Free Liquid Cylinders," *J. Chem. Soc., Faraday Trans. I*, **70**, 1228 (1974).

Chang, H.-C., "Wave Evolution on a Falling Film," *Annu. Rev. Fluid Mech.*, **26**, 103 (1994).

Chang, H.-C., and E. A. Demekhin, *Complex Wave Dynamics on Thin Films*, Elsevier, Amsterdam, The Netherlands (2002).

Chang, H.-C., M. Cheng, E. A. Demekhin, and D. I. Kopelevich, "Secondary and Tertiary Excitation of Three-Dimensional Patterns on a Falling Film," *J. Fluid Mech.*, **270**, 251 (1994).

Chang, H.-C., E. A. Demekhin, and E. Kalaidin, "Simulation of Noise-Driven Wave Dynamics on a Falling Film," *AIChE J.*, **42**, 1553 (1996a).

Chang, H.-C., E. A. Demekhin, E. Kalaidin, and Y. Ye, "Coarsening Dynamics of Falling-Film Solitary Waves," *Phys. Rev. E*, **54**, 1467 (1996b).

Chang, H.-C., E. A. Demekhin, and D. I. Kopelevich, "Nonlinear Evolution of Waves on a Vertically Falling Film," *J. Fluid Mech.*, **250**, 433 (1993a).

Chang, H.-C., E. A. Demekhin, and D. I. Kopelevich, "Construction of Stationary Waves on a Falling Film," *Comput. Mech.*, **11**, 313 (1993b).

Chang, H.-C., E. A. Demekhin, and S. S. Saprikin, "Noise-Driven Wave Transitions on a Vertically Falling Film," *J. Fluid Mech.*, **462**, 255 (2002).

Cheng, M., and H.-C. Chang, "Competition Between Subharmonic and Sideband Secondary Instabilities on a Falling Film," *Phys. Fluids*, **7**, 34 (1995).

Dias, F., and C. Kharif, "Nonlinear Gravity and Capillary-Gravity Waves," *Annu. Rev. Fluid Mech.*, **31**, 301 (1999).

Emmert, R. E., and R. L. Pigford, "A Study of Gas Absorption in Falling Liquid Films," *Chem. Eng. Prog.*, **50**, 87 (1954).

Feind, K., "Strömungsuntersuchungen bei Gegenstrom von Rieselfilmen und gas in lotrechten Rohren," VDI-Forschungsheft, Vol. 481 (1960).

Fulford, G. D., "The Flow of Liquids in Thin Films," *Adv. Chem. Eng.*, **5**, 151 (1964).

Hikita, H., K. Nakanishi, and T. Kataoka, "Liquid Phase Mass Transfer in Wetted-Wall Columns," (in Japanese), *Chem. Eng.*, **23**, 459 (1959).

Himmelblau, D. M., "Diffusion of Dissolved Gases in Liquid," *Chem. Rev.*, **64**, 527 (1964).

Ho, L. W., and A. T. Patera, "A Legendre Spectral Element Method for Simulation of Unsteady Incompressible Viscous Free-Surface Flows," *Comput. Methods Appl. Mech. Eng.*, **80**, 355 (1990).

Jackson, L. J., "Liquid Films in Viscous Flow," *AIChE J.*, **1**, 231 (1955).

Joo, S. W., and S. H. Davis, "Instabilities of Three-Dimensional Viscous Falling Films," *J. Fluid Mech.*, **242**, 529 (1992a).

Joo, S. W., and S. H. Davis, "Irregular Waves on Viscous Falling Films," *Chem. Eng. Commun.*, **118**, 111 (1992b).

Joo, S. W., S. H. Davis, and S. G. Bankoff, "Long-Wave Instabilities of Heated Falling Films: Two-Dimensional Theory of Uniform Layers," *J. Fluid Mech.*, **230**, 117 (1991).

JSME Data Book, *The Thermophysical Properties of Fluids*, Japan Society for Mechanical Engineers, Tokyo, Japan, p. 208 (1986).

Kamei, S., and J. Oishi, "Mass and Heat Transfer in a Falling Liquid Film of Wetted Wall Tower," *Memoirs Fac. Eng., Kyoto Univ.*, **17**, 277 (1956).

Kapitza, P. L., and S. P. Kapitza, "Wave Flow of Thin Layers of a Viscous Fluid: III. Experimental Study of Undulatory Flow Conditions," *Collected Papers of P. L. Kapitza*, Vol. 2, D. Ter Haar, ed., Pergamon, New York, p. 690 (1965).

Karimi, G., and M. Kawaji, "An Experimental Study of Freely Falling Films in a Vertical Tube," *Chem. Eng. Sci.*, **53**, 3501 (1998).

Krist, S. E., and T. A. Zang, "Numerical Simulation of Channel Flow Transition," NASA Tech. Pap. 2667 (1987).

Lamourelle, A. P., and O. C. Sandall, "Gas Absorption into a Turbulent Liquid," *Chem. Eng. Sci.*, **27**, 1035 (1972).

Lasheras, J. C., and H. Choi, "Three-Dimensional Instability of a Plane Free Shear Layer: An Experimental Study of the Formation and Evolution of Streamwise Vortices," *J. Fluid Mech.*, **189**, 53 (1988).

Liu, J., and J. P. Gollub, "Solitary Wave Dynamics of Film Flows," *Phys. Fluid*, **6**, 1702 (1994).

Liu, J., J. D. Paul, and J. P. Gollub, "Measurements of the Primary Instabilities of Film Flows," *J. Fluid Mech.*, **250**, 69 (1993).

Liu, J., J. B. Schneider, and J. P. Gollub, "Three Dimensional Instabilities of Film Flows," *Phys. Fluids*, **7**, 55 (1995).

Miyara, A., "Numerical Simulation of Wavy Liquid Film Flowing Down on a Vertical Wall and an Inclined Wall," *Int. J. Thermal Sci.*, **39**, 1015 (2000).

Nagasaki, T., H. Akiyama, and H. Nakagawa, "Numerical Analysis of Flow and Mass Transfer in a Falling Liquid Film with Interfacial Waves," *Thermal Sci. Eng.*, **10**, 17 (2002).

Nagasaki, T., and K. Hijikata, "A Numerical Study of Interfacial Waves on a Falling Liquid Film," *ANS Proc. National Heat Transfer Conf.*, **4**, 23 (1989).

Nakoryakov, V. E., B. G. Pokusaev, and S. V. Alekseenko, "Effect of Waves on the Desorption of CO_2 from Flowing Liquid Films," *Theor. Found. Chem. Eng.*, **17**, 199 (1983).

Nishioka, M., M. Asai, and S. Iida, "Wall Phenomena in the Final Stage of Transition to Turbulence," *Transition and Turbulence*, R. E. Meyer, ed., Academic Press, New York, p. 113 (1981).

Nosoko, T., P. N. Yoshimura, T. Nagata, and K. Oyakawa, "Characteristics of Two-Dimensional Waves on a Falling Liquid Film," *Chem. Eng. Sci.*, **51**, 725 (1996).
Ooshida, T., "Surface Equation of Falling Film Flows with Moderate Reynolds Number and Large but Finite Weber Number," *Phys. Fluids*, **11**, 3247 (1999).
Pierson, F. W., and S. Whitaker, "Some Theoretical and Experimental Observations of the Wave Structure of Falling Liquid Films," *Ind. Eng. Chem. Fundam.*, **16**, 401 (1977).
Pumir, A., P. Manneville, and Y. Pomeau, "On Solitary Waves Running Down an Inclined Plane," *J. Fluid Mech.*, **135**, 27 (1983).
Ramaswamy, B., S. Chippada, and S. W. Joo, "A Full-Scale Numerical Study of Interfacial Instabilities in Thin-Film Flows," *J. Fluid Mech.*, **325**, 163 (1996).
Roberts, R. M., and H.-C. Chang, "Wave Enhanced Interfacial Transfer," *Chem. Eng. Sci.*, **55**, 1127 (2000).
Rumscheidt, F. D., and S. G. Mason, "Break-Up of Stationary Liquid Threads," *J. Colloid Sci.*, **17**, 260 (1962).
Salamon, T. R., R. C. Armstrong, and R. A. Brown, "Traveling Waves on Vertical Films: Numerical Analysis Using the Finite Element Method," *Phys. Fluids*, **6**, 2202 (1994).
Seban, B. R., and A. Faghri, "Wave Effects on the Transport to Falling Laminar Liquid Films," *J. Heat Transfer*, **100**, 143 (1978).
Tamir, A., and Y. Taitel, "Diffusion to Flow Down an Incline with Surface Resistance," *Chem. Eng. Sci.*, **26**, 799 (1971).
Trifonov, Yu. Ya., "Bifurcations of Two-Dimensional into Three-Dimensional Wave Regimes for a Vertically Flowing Liquid Film," *Fluid Dyn.*, **25**, 741 (1991).
Truesdale, G. A., A. L. Downing, and G. F. Lowdan, "The Solubility of Oxygen in Pure Water and Sea-Water," *J. Appl. Chem.*, **5**, 53 (1955).
Tsvelodub, O. Yu., and Yu. Ya. Trifonov, "Nonlinear Waves on the Surface of a Falling Film. Part 2. Bifurcations of the First-Family Waves and Other Types of Nonlinear Waves," *J. Fluid Mech.*, **244**, 149 (1992).
Vazquez-Una, G., F. Chenlo-Romero, M. Sanchez-Barral, and V. Perez-Munuzuri, "Mass-Transfer Enhancement Due to Surface Wave Formation at a Horizontal Gas-Liquid Interface," *Chem. Eng. Sci.*, **55**, 5851 (2000).
Yih, C. S., "Stability of Liquid Flow Down an Inclined Plane," *Phys. Fluids*, **6**, 321 (1963).
Yoshimura, P. N., T. Nosoko, and T. Nagata, "Enhancement of Mass Transfer into a Falling Laminar Liquid Film by Two-Dimensional Surface Waves—Some Experimental Observations and Modeling," *Chem. Eng. Sci.*, **51**, 1231 (1996).

Manuscript received Jan. 21, 2003, and revision received Mar. 19, 2003.